Exploring the optical and energetic properties of a Co(II)-based mixed ligand MOF

Dhouha Abid, Issam Mjejri, Rim Jaballi, Philippe Guionneau, Stanislav Pechev, El-Kebir Hlil, Nathalie Daro, Zakaria Elaoud

To cite this version:

Dhouha Abid, Issam Mjejri, Rim Jaballi, Philippe Guionneau, Stanislav Pechev, et al.. Exploring the optical and energetic properties of a Co(II)-based mixed ligand MOF. Inorganic Chemistry, 2024, 63 (14), pp.6152-6160. ⟨10.1021/acs.inorgchem.3c03638⟩. ⟨hal-04538796⟩

HAL Id: hal-04538796
https://hal.science/hal-04538796v1

Submitted on 9 Apr 2024

Exploring the Optical and Energetic Properties of a Co(II)-based mixed ligand MOF

Dhouha ABID [a*], Issam MJEJRI [b*], Rim JABALLI [a], Philippe GUIONNEAU [c], Stanislav PECHEV [c], El kebir HLIL [d], Nathalie DARO [c], Zakaria ELAOUD [a]

[a] Laboratory Physical-Chemistry of Solid state, University of Sfax, Faculty of Sciences of Sfax, Tunisia, BP 802, Route de Soukra, 3018 Sfax, Tunisia.

[b] Unit of Materials and Environement (UR15ES01), IPEIT, University of Tunis, 2 rue Jawaher Lel Nahru, 1089, Montfleury, Tunisia.

[c] Univ. Bordeaux, CNRS, Bordeaux INP, ICMCB, UMR 5026, F-33600 Pessac, France.

[d] Institut Neel, CNRS - Université J. Fourier, BP. 166, 38042 Grenoble, France.

***Corresponding Author:**

Dhouha ABID, dhouhaabid20@gmail.com

Issam MJEJRI, mjejriissam@gmail.com

Abstract

Due to their remarkable properties, including remarkable porosity and extensive surface area, Metal–organic frameworks (MOFs) are being investigated for various applications. Herein, we report the first Co(II)-based mixed ligand MOF, formulated $Co_4(HTrz)_2(D\text{-}cam)_{2.5}(\mu\text{-}OH)_3$. Its 3D structure framework is composed of helical chains $\{[Co_4(\mu_3\text{-}HTrz)_4]^{8+}\}_n$ connected by D-camphorate ligand building blocks and featured as an extended structure in AB-AB fashion. The investigated compound displays a wide absorption range across the visible spectrum, characterized by an optical gap energy of 3.7 eV, indicating its semiconducting nature and efficient sunlight absorption capabilities across various wavelengths. The electrochemical performance demonstrated an excellent reversibility, cyclability, structural stability, as well as a specific capacity of up to100 cycles at a scan rate of 0.1 mV. s^{-1} and a current density of 50 mA. g^{-1}. Thus, showcasing its ability to retain the capacity over numerous charge-discharge cycles. Additionally, the investigated sample displayed impressive rate capability during the Li-ion charge/discharge process. Therefore, the material's remarkable electrochemical properties can be ascribed to the synergistic effects of its large specific surface area of 348.294 m^2. g^{-1} and well-defined pore size distribution of 20.448 Å, making it a promising candidate for high-performance Li-ion batteries.

KEYWORDS: Metal−organic framework (MOF), porous structure, optical analysis, cathode material, lithium-ion batteries, BET surface analysis.

Introduction

The growing worldwide need for energy coupled with the depletion of the remaining reserves of fossil fuels has sparked numerous efforts toward developing sustainable energy alternatives. Electrical energy storage (EES) has been identified as one of the most promising technologies to produce fuels in a clean, efficient, and cost-effective manner [1-4]. Due to their long lifespan, excellent cycling stability, and environmental friendliness, Lithium-Ion Batteries (LIBs) are one of the EES technologies that are being developed to fulfill the increasing demand for sustainable energy. However, an in-depth investigation has demonstrated that the electrode materials play a crucial role in the performance of lithium-based batteries. Finding appropriate electrode materials with high electronic conductivity, a large specific surface area, high efficiency, and great electrochemical performance is the major challenge towards developing efficient LIBs storage systems. [5-13]. Currently, several materials have been investigated as LIB electrodes, including metal oxide [14-18], graphene [19-21], carbon nanotubes [22-24], and so on. Due to their superior electrical conductivity and large pore volume, these materials are considered as a good electrodes or support materials for lithium-based batteries. Their comparatively low cycle life and rate capacity, however, have prevented them from meeting the growing market demand. Particularly, metal-organic frameworks (MOFs) have garnered considerable interest as potential electrode materials for lithium-ion rechargeable batteries (LIBs). Porous MOFs are formed through the self-assembly of metal nodes and clusters connected by organic ligands, marking them a promising electrode materials for LIBs. Owing to their good chemical stability, significant surface area, and ultrahigh porosity, they benefit from the assemblage of metal clusters and organic ligands, making them an ideal electrode candidate. Additionally, porous MOF materials exhibit several benefits when exploited as electrodes in lithium-based batteries [25-30] : (i) Their porous structure allows for the penetration of electrolytes ; (ii) their tunable surface and structure are exploited to optimize their performance ; (iii) their highly flexible components assure the incorporation of electro-active sites [31-33]. In 2006, L. Xiaoxia and colleagues investigated the first Zn-MIL-177- MOF anode materials with the general formula $Zn_4O(C_9H_6O_6)_2$ [34] for rechargeable lithium-ion batteries. However, due to its poor cycling stability, the electrochemical performance of MOF-177 for Li-ion storage was insufficient. Since then, additional experimental research of porous MOF electrode materials has been reported. The $Co_2(OH)_2BDC$ MOF [35] material synthesized by G. Lei's group demonstrated good reversible capacity of 650 mAh. g^{-1} along with an impressive cyclic stability at a current density of 50 mA. g^{-1}. Yamada's group also investigated a porous organometallic material, namely MIL-101(Fe) [36], that demonstrated impressive lithium storage performance, a good charge-discharge capacitance with a rate performance of 110 mAh. g^{-1} and excellent cycling stability upon 100 cycles. The Mn (tfbdc) (4,4′-bpy) $(H_2O)_2$ [37] porous complex exhibited a remarkable storage capacity of lithium ions of 390 mAh. g^{-1} over 50 cycles. Recently, in 2022, J. Geng and co-workers synthesized a novel 2D MOF with the formula Fe-TABQ (TABQ: tetra-amino-benzoquinone) [38] that delivers over 95% capacity retention after 200 cycles. Aside from these fascinating electrochemical characteristics, these MOFs materials have exhibited compelling optical and magnetic properties, expanding the range of their potential applications, especially in light LED and Solar cells.

In the present study, we report a new 3-D Co(II)-MOF constructed from D-camphoric acid and N-donor 1H-1,2,4-triazole as an auxiliary ligand, namely, $Co_4(HTrz)_2(D\text{-}cam)_{2.5}(\mu\text{-}OH)_3$, as an active cathode material for lithium-ion storage. The crystal structure characteristics, thermal, spectroscopic, optical analyses were studied. Furthermore, the synthesized Co(II)-based MOF was electrochemically evaluated to investigate its charge-discharge capacity, stability and rate performance during the lithium-ion insertion and extraction processes.

II. EXPERIMENTAL SECTION

II. 1. Synthesis of $Co_4(HTrz)_2(D\text{-}cam)_{2.5}(\mu\text{-}OH)_3$ MOF

The chemical reagents, including cobalt (II) nitrate hexahydrate ($Co(NO_3)_2.6H_2O$, 98%), 1,2,4-triazole ($C_2H_3N_3$, 98%), and (1R,3S)-(+)-Camphoric acid ($C_{10}H_{16}O_4$, 99%), have been purchased from Sigma-Aldrich and were utilized without any additional purification.

After screening various chemical reaction parameters of the hydrothermal conditions, such as time (e.g. 2, 3, 5 days), temperature (e.g.120, 140, 160 °C), pH, solvent (e.g. ethanol, water, methanol, DMF), counter-anion of the metal (NO_3^{2-}, Cl^-, ClO_4^-) and molar ration (e.g.1:1:1, 0.5:1:1), purple needle-shaped crystals were collected according to the following synthesis: An aqueous solution of $Co(NO_3)_2.6H_2O$(29 mg, 1 mmol) was added gradually to an ethanolic solution D-camphoric acid (15 mg, 0.75 mmol) and HTrz (48 mg, 0.75 mmol) with stirring. The obtained solution of the ternary mixture was neutralized using 0.1 mol L^{-1} KOH, transferred to a stainless-steel autoclave, and then heated to 160°C for 5 days. The resulting crystals were thoroughly washed with water and allowed to air-dry at ambient temperature.

The scanning electron microscopy (SEM) image reveals that Co-MOF particles exhibit needle-shaped morphology **(Fig S1)**.

II. 2. Chemical characterizations

Using a polarizing microscope, an appropriate crystal of Co-MOF had been carefully selected, and mounted on a Bruker Kappa APEX II diffractometer using Mo-K radiation, intensity data were gathered within the range $1.3° \leq \theta \leq 27.5°$. A total of 45830 reflections were recorded, among which 7030 had an intensity of $I > 2\ \sigma(I)$.

The crystal structure was determined in the triclinic system, adopting the centrosymmetric space group P-1. Metallic cobalt atoms were determined using the Patterson method, implemented in the SHELXS-97 program **[39]** included in the WINGX software **[40]**. The remaining atoms, including carbon, oxygen, and nitrogen, were identified through successive Fourier calculations and refined in the concluding cycles with anisotropic thermal parameters using the SHELXL-2018 program **[41]**. Hydrogen atom positions were calculated using a riding model, with N–H = 0.89 Å and C–H = 0.93 Å. Following multiple refinements, the final reliability factors were determined as $R_1 = 0.068$ and $wR_2 = 0.179$. Packing diagrams were drown using the Diamond 4.6 program **[42]**

Table S1 gathers all the crystallographic characteristics and structure refinement details of the complex. Atomic positional parameters as well as anisotropic factors (Ueq/ Uiso) are listed in **Tables S2 and S3**, respectively. Inter-atomic distances and bond angles are depicted in **Table S4**.

BET measurement of nitrogen adsorption isotherms measured at 77 K was carried out using the ASAP 2020 Micrometrics Surface Area and Porosity Analyzer. The title compound was pre-treated under vacuum for 4 hours at 120°C in order to remove any guest molecules before the BET analysis.

Thermogravimetric analysis was carried out by heating 3.2 mg of powdered sample in air at temperatures ranging from 30.00 to 450.00 °C at a rate of 10.00 °C min^{-1}.

FT-Infrared analysis were performed at room temperature using a Perkin-Elmer FT-IR in the frequency range of 400-4000 cm^{-1}. The Co-MOF was pressed into pellets after dilution in KBr.

II. 3. Optical measurements

Diffuse reflectance measurements were performed on polycrystalline powder samples under ambient conditions. These measurements covered a wavelength range of 250 to 1100 nm and were conducted using a PerkinElmer Lambda 750 UV/VIS/NIR spectrometer.

II. 4. Electrochemical measurements

The different cathodes have been fabricated from a mixture of Co(II)-based MOF, acetylene black, and PVDF in N-methyl-2-pyrrolidone (NMP) solvent. The slurry was thoroughly mixed by sonication and then coated onto aluminum foil using the doctor-blading method. The coated electrodes were dried in vacuum at 120 °C for 12 hours, followed by cutting into small disks. The mass loading of the active materials was approximately 2.1 mg per electrode. To enhance the electrical contact between the aluminum foil and active material, the electrodes were pressed after drying. After optimizing the cathode material, coin-type cells (CR2032) were assembled in an argon-filled glove box. Li foils served as the anodes, while a microporous polyethylene film acted as the separator. The electrolyte solution was prepared with 1 M LiPF6 in a mixture of ethylene carbonate (EC), diethylene carbonate (DEC), and dimethyl carbonate (DMC) in a volume ratio of 1:1:1.

Galvanostatic charge-discharge experiments were conducted on all cells using a Neware multi-channel battery system with different current densities. These tests were performed in the voltage range of 3.0-1.0 V. Cyclic voltammetry analysis was carried out using a BioLogic SP150, exploring the potential range from 1.0 to 3.0 V.

III. RESULTS AND DISCUSSION

III. 1. Crystal structure description

The SCXRD investigation revealed that the Co(II)-based material is composed of a neutral tetra-nuclear complex which crystallizes in the triclinic system and adopts the centrosymmetric space group P-1 and features a unique porous 3-D structure. As reported in **Figure 1.a**, the asymmetric unit is composed of four divalent cobalt atoms, two and a half of deprotonated D-Cam ligands, two fully deprotonated HTrz ligands, three coordinated hydroxide anions and one guest of nitrate anion (μ_1-NO_3). It is noteworthy to note that all atoms full a general position and a Wyckoff site (2i). As depicted in **Figure 1.b**, four Co(II) sites exhibit two different coordination geometries. In fact, cobalt atoms Co_1 and Co_2 are six-coordinated in an $\{N_2O_4\}$ environment. Within the Co_1 polyhedral, the equatorial plane is composed of two donor nitrogen atoms from different HTrz ligands and two oxygen atoms from different D-cam ligands, while the axial plane is formed from two oxygen atoms derived from different hydroxyl anions. For the Co_2(II) center, the equatorial plane is filled with one nitrogen atom derived from the HTrz ligand, one carboxylate oxygen atom, one oxygen atom derived from the hydroxyl anion, and one oxygen atom derived from the nitrate group. The additional nitrogen and oxygen atoms from different HTrz and D-cam ligands are situated in the axial sites. The Co_1/CO_2 -N bond distances are ranging from 2.073 (7) to 2.144 (7), and the Co_1/Co_2 -O bond lengths range from 2.034 (5) to 2.242 (8), resulting in distorted octahedral geometry and typical axial elongation. This phenomenon can be attributed to the Jahn-Teller effect. The computed average values of the distortion indices are $ID_{d(M-L)} = 0.038$ and 0.045, respectively, for Co_1 and Co_2 octahedral ($ID_d = \sum\left(\left|\frac{di-dm}{n.dm}\right|\right)$ (eq. 1)), where ; di is the metal-ligand bond length). Cobalt atoms Co_3 and Co_4 are penta-coordinated in $\{NO_4\}$ environments.

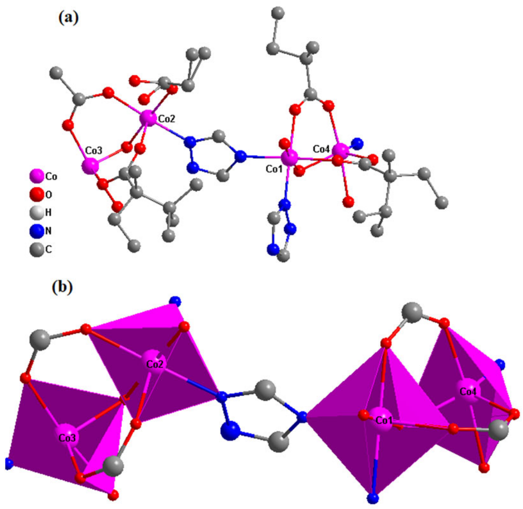

Figure 1. **(a)** Asymmetric unit of the MOF $Co_4(HTrz)_2(D\text{-}cam)_{2.5}(\mu\text{-}OH)_3$, for more clarity, the hydrogen atoms have been omitted, **(b)** Coordination sphere of cobalt centers.

The Addison trigonality factors τ calculated for the cobalt atoms Co_3 (II) and Co_4 (II) using the equation $\tau = (\beta - \alpha)/ 60$ (eq.2) are 0.2888 and 0.54785 Å, respectively. Such results indicate that the Co_3(II) atom adopts distorted square pyramidal geometry, whereas, the Co_4(II) atom adopts an intermediate geometry between the square pyramidal and trigonal bipyramid configurations. Within these polyhedral, one HTrz nitrogen atom (N_4 and N_2, respectively, for Co_3 and Co_4 atoms) comprises the apical positions, while two carboxylate oxygen atoms deriving from different deprotonated D-cam ligands and two oxygen atoms from hydroxyl anions fill the basal planes. The Co_3/Co_4–O and Co_3/Co_4–N bond lengths vary between 1.983 (5)-1.989 (5) Å and 2.051 (7), 2.052 (7) Å, respectively. These bond distances are close to those previously reported for Co(II)-based complexes [42-47]. While investigating bond angles, attention should be drawn to the intermetallic distances. In fact, $d_{Co1...Co4}$ and $d_{Co2...Co3}$ are of the order of 3.415 Å and 3.219 Å (**Fig. 1.b**) and Co_1-O_1-Co_4 and Co_2-O_8-Co_3 bridging angles are 105(3)° and 116.4(1)°, respectively, which may reflect interesting magnetic properties. Each HTrz ring exhibits μ_3:η^1:η^1:η^1 binding fashion, bridging three cobalt sites through its N_1, N_2 and N_4 donor groups [48-51]and generating infinite double left-right handed helical chains occurring along the [010] direction (**Fig. 2**). Additionally, the D-cam adopts $\mu_4–\eta^1:\eta^1:\eta^1:\eta^1$ and $\mu_2–\eta^1:\eta^1$ binding modes, bridging a pair of Co(II) atoms via its carboxylate groups. These latter units are arranged in an AB-AB fashion and further interconnect the HTrz double-helix to generate an overall 3-D helical network with the nearest inter-helix distance of 9.38Å.

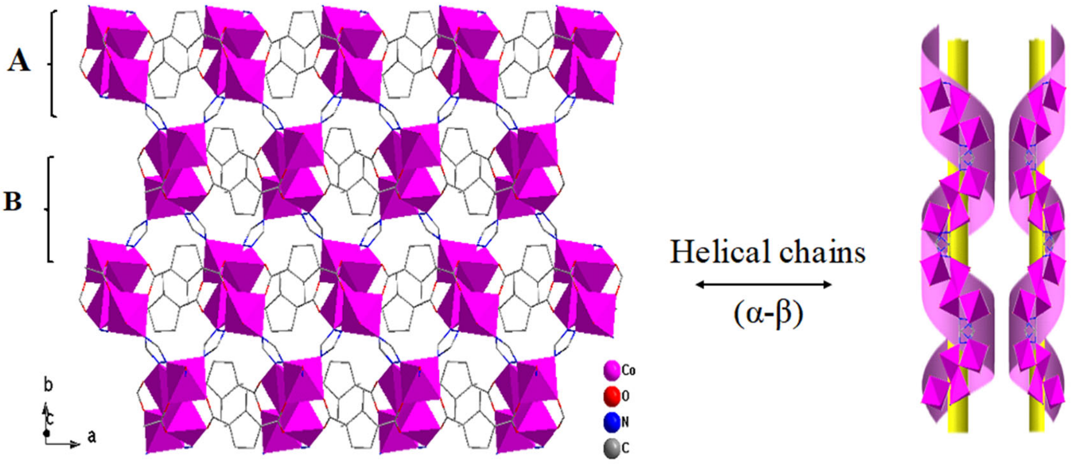

Figure 2. Atomic arrangement of the title complex along the (*a, b*) plane with representation of the α- β helix.

From a topological approach, each D-cam and HTrz ligand links three cobalt centers that can be considered as three-connecting nodes. Thus, the 3-D framework results in an unprecedented trinodal (4,3)-connected topology and a Schläfli symbol of $(3^{12}4^{18}5^{6})$ $(3^{9}4^{16}5^{3})$ [52,53]. As presented in **Figure 3**, the pore size of the spheres is of the order of 12.750 Å.

Since the unit cell volume of the hole frameworks is of the order of 2033.1 Å^3, the void volume accessible for different guest species evaluated using the PLATON SQUEEZE program corresponds to a potential porosity of 27.5% (558.7 Å^3).

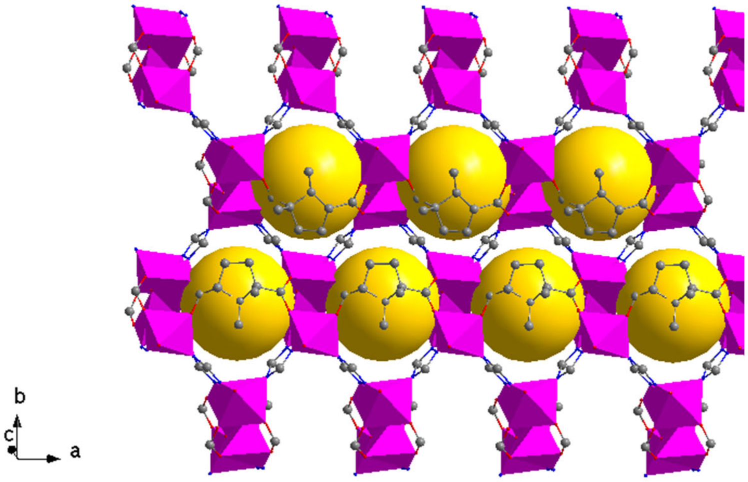

Figure 3. 3-D structure of the porous complex, where orange spheres presents the void accessible volume.

III.2. BET analysis

Nitrogen adsorption and desorption measurements at 77 K were performed to characterize the specific surface area and pore size of the activated Co-MOF. The results demonstrated a large specific BET surface area of 348.294 m^2 g^{-1} and a total pore size of 20.448 Å. These exceptional characteristics are significantly superior to those reported for other MOF systems, suggesting that the activated Co-MOF holds great potential for energy storage applications. In addition, according to the N_2 isotherm, we note that the desorption curves do not overlap with the adsorption curve, revealing a type IV isotherm and indicating the microporous size distribution. **Figure 4** illustrates the N_2 Adsorption/Desorption isotherm of the porous MOF.

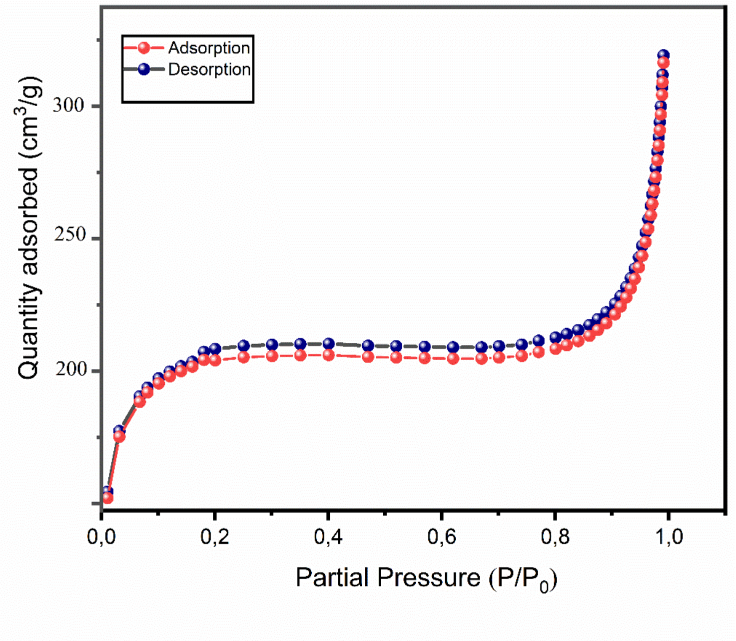

Figure 4. Adsorption/Desorption isotherm of azote at 77 K of the Co(II)-based title complex.

III. 3. Thermal stability and FT-IR Spectroscopy

The TGA curve for the Co-based MOF **(Fig. S2)** revealed a two-step decomposition process. The initial weight loss between 71 and 101.08°C, accounting for 2.8% of the original mass, is attributed to the release of hydroxyl ions from the material. Subsequently, a more significant weight loss occurs between 118.3°C and 430°C, representing the decomposition of the structure network and the formation of CoO as a final residue.

Figure S3 illustrates the FT-IR spectrum recorded at room temperature. Band assignments are determined by examining previously reported similar complexes [35-39,45,46]. The observed weak band at 3630 cm^{-1} is assigned to the stretching vibration of the hydroxide ligand and N–H stretching. The two broad bonds observed at 2930 and 2880 cm^{-1} are assigned to the C-H vibration of HTrz [50-52] and D-camp ligands, respectively. In addition, symmetric and asymmetric C=O stretching peaks of the D-camp ligand appear at around 1680 cm^{-1}. The characteristic bond at 1560 cm-1 is ascribed to the δ (NH_2) bending mode. Medium-intensity peaks observed in the range of 1530-1480 cm^{-1} are assigned to the asymmetric and symmetric deformation of the C-C [54-57] bond within the D-camp group. A series of sharp, medium peaks ranging from 1390 to 670 cm^{-1} are ascribed to the vibration modes of the aromatic HTrz skeleton. The Co-O bending mode gives rise in the IR spectrum to a medium bond at around 470 cm^{-1} [58].

III. 4. Optical investigation

Solid-state room-temperature diffuse reflectance measurements were carried out over a 250−800 nm range. The data was converted to absorption spectra using the Kubelka-Munk (K.M) remission function [53,58]:

$$F(R) = \alpha/S = ((1-R)^2)/2R. \qquad \text{(eq.4)}$$

Where; S: the scattering coefficient, α: the absorption coefficient, and R: the complex's reflectance.

Figure 5. a shows the normalized reflectance spectrum of the Co-MOF measured at room temperature. The spectrum reveals an intense absorption band in the UV region around 304 nm (4.07 eV) and a shoulder one around 402 nm (3.04 eV). These bands are associated with the π-π* or n-π* transitions of the HTrz aromatic ligand and to the transition from BV to BC of the inorganic excitons confined within the Co(II)-based polyhedron, respectively. The deconvolution of the normalized reflectance spectrum (**Fig 5. b**) in the spectral region between 450 and 750 nm reveals the presence of one shoulder at 539 nm (2.3 eV) followed by two Gaussian shaped peaks at 576 nm (2.15 eV) and 633 nm (1.9 eV). These bonds are associated with the d-d electronic transitions within the Co^{2+} ions. According to the Tanabe-Sugano diagram, three spin allowed peaks are anticipated. The first bond at 539 nm is the transition from the $^4A_2$ (F) ground term to the $^4T_2$(F), the second bond at around 576 nm corresponds to the transitions from $^4A_2$(F) ground term to the $^4T_1$(F), and the last bond at 633 nm corresponds to the transition from the ^{4} A_2(F) ground term $^4T_1$(P) [52-60].

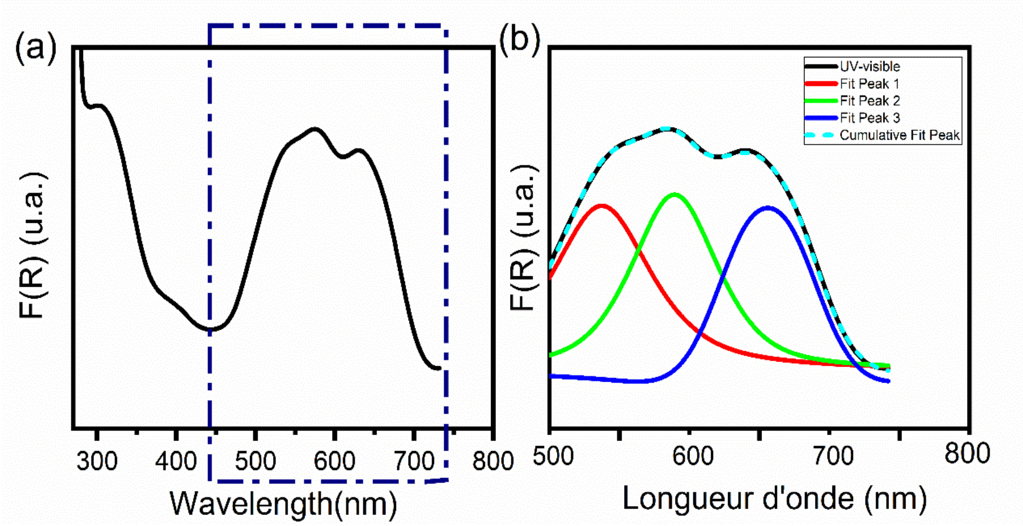

Figure 5. (a) The normalized reflectance spectrum F(R) of the Co (II)-MOF measured at room temperature, **(b)** The deconvolution of the normalized reflectance spectrum between 450-750 nm.

The optical gap energy of the complex is calculated from the following equation [61,62]:

$$[F(R)\, h\nu] = A\, (h\nu - Eg)^n \qquad \text{(eq.5)}$$

Where; h and ν represent the Planck constant and photon frequency, A is a constant unrelated to energy, Eg is the optical band gap, and n is a constant defining the nature of optical transitions. In the case of a direct transition (n = 1/2), the energy associated with the direct gap is designated as Eg_d. In contract, for an indirect transition (n = 2), the energy corresponding to the indirect gap is referred to as Eg_{in}.

Figure 6. a, **b** depict the variation of $(F(R)h\nu)^2$ and $(F(R)h\nu)^{1/2}$ versus energy (hν). The determination of direct and indirect gap energies involved extrapolating the linear portion of the curve to the *x*-axis. The calculated values for Eg(d) and Eg(in) are approximately 2.7 eV and 3.7 eV, respectively.

The slope obtained from the Ln F(R)hν versus Ln(hν-Eg) plot in **Figure 6. c, d** yields a value of n equal to 2, confirming an indirect transition. Therefore, the optical gap energy value allows us to classify the studied porous MOF as a semiconductor and confirms that it is a good candidate for interesting photo-active devices [52-62].

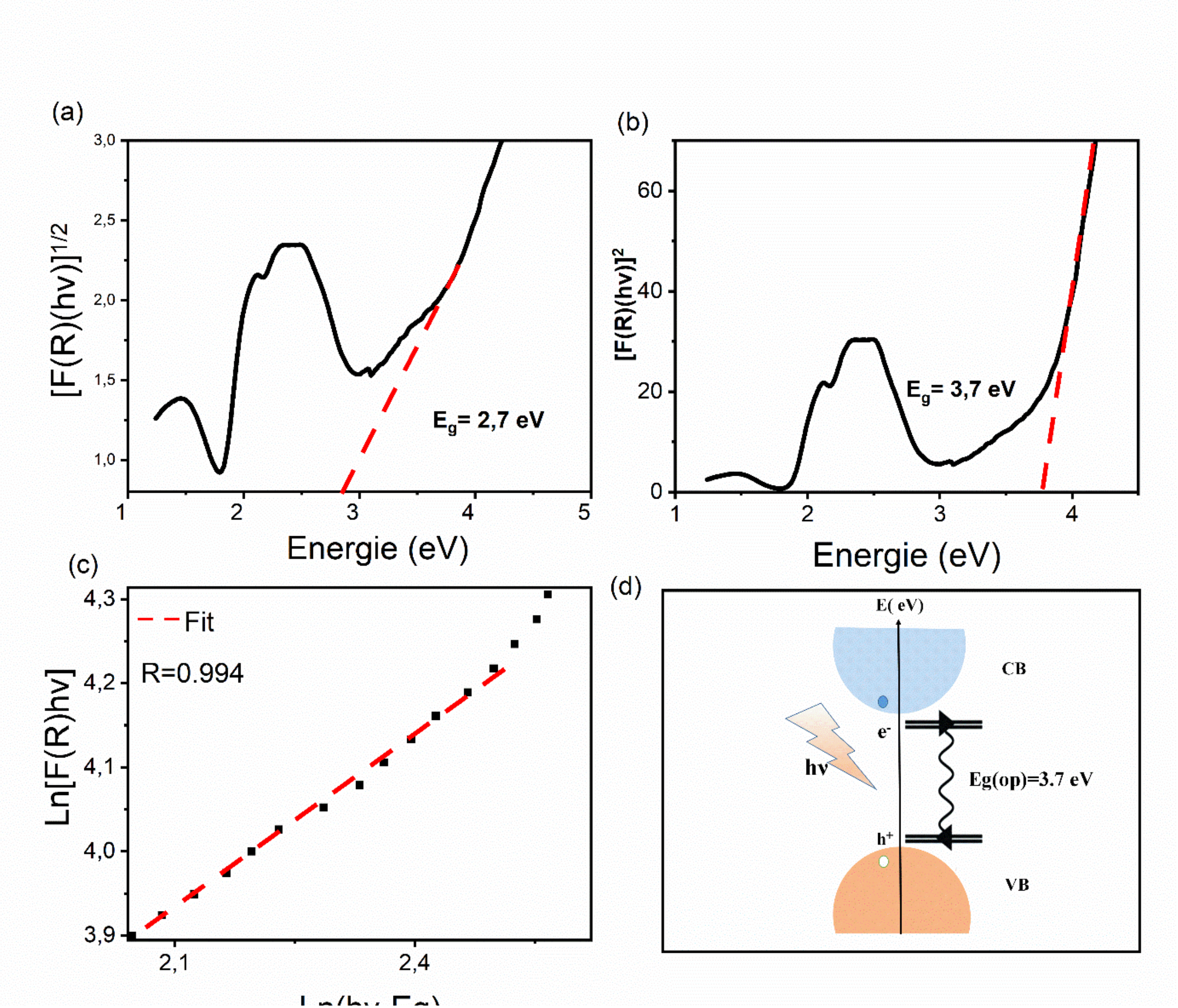

Figure 6. The variation of **(a)** $(F(R)\ h\nu)^2$ and **(b)** $(F(R)\ h\nu)^{1/2}$ as a function of the energy (hν), **(c)** The variation of Ln(F(R) hν versus Ln(hν-Eg), **(d)** Energy diagram of the solid-sate optical absorption mechanism of the investigated Co-MOF.

III. 5. Electrochemical study

For a deep investigation of the electrochemical performance of the new compound-based MOF as cathodes in LIBs, coin cell 2032 type of $Co_4(HTrz)_2(D\text{-}cam)_{2.5}(\mu\text{-}OH)_3$ against lithium metal electrode was constructed and operated using cyclic voltammetry (CV) and galvanostatic charge/discharge (GCD) technique within a voltage range spanning 1.0 to 3.0 V. **Figure 7** reveals the relative cyclic voltammograms (CVs) of the $Co_4(HTrz)_2(D\text{-}cam)_{2.5}(\mu\text{-}OH)_3$ electrode cycled at a scan rate of 0.1 mV s^{-1} within the potential window of 1.0–3.0 V. The analysis of cyclic voltammograms (CVs) for the composite material as a cathode reveals multiple cathodic and anodic peaks, indicative of various lithium ion intercalation and de-intercalation processes within the cathode, respectively. The voltammograms exhibit a significant current wave upon reduction, which consists of three main cathodic peaks at 2.77

V, 2.26 V, and 1.53 V. These laters are attributed to the distinct phase transformation from $Co_4(HTrz)_2(D\text{-}cam)_{2.5}(\mu\text{-}OH)_3$ to $Li_xCo_4(HTrz)_2(D\text{-}cam)_{2.5}(\mu\text{-}OH)_3$.

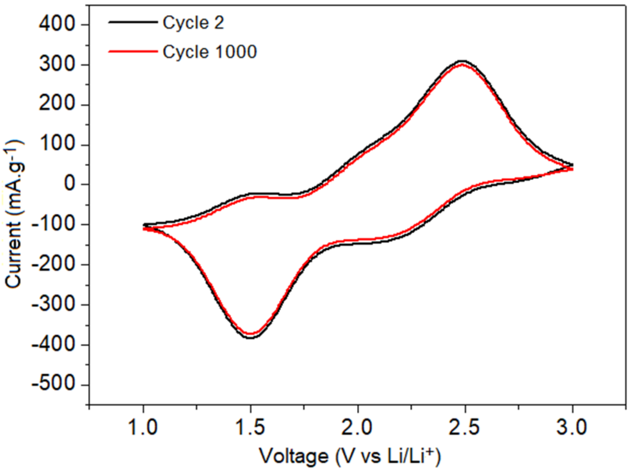

Figure 7. Cyclic voltammetry (CV) profiles for $Co_4(HTrz)_2(D\text{-}cam)_{2.5}(\mu\text{-}OH)_3$ were obtained at a scan rate of 0.1 mVs^{-1} within the voltage range from 1 V to 3 V (vs Li$^+$/Li).

We noticed that during the oxidation process, three distinct anodic peaks were identified. The peaks observed at 1.57 V, 2.03 V, and 2.51 V are attributed to the de-intercalation of Li^+ ions. These peaks correspond to the reverse phase transformations from $Li_xCo_4(HTrz)_2(D\text{-}cam)_{2.5}(\mu\text{-}OH)_3$ to $Co_4(HTrz)_2(D\text{-}cam)_{2.5}(\mu\text{-}OH)_3$ respectively. The remarkable performance of new cobalt (II) complex-based MOF cathode is attributed to several factors: (i) the highly porous material with pore diameters about 100 nm which facilitates the insertion/extraction of the lithium, (ii) the material's important specific surface area and enhanced conductivity, (iii) the nanostructure aspect of the $Co_4(HTrz)_2(D\text{-}cam)_{2.5}(\mu\text{-}OH)_3$ powder which contributed to the highly reactive surface. The electrochemical performance of $Co_4(HTrz)_2(D\text{-}cam)_{2.5}(\mu\text{-}OH)_3$ as a cathode material for Lithium-ion Batteries (LIBs) was evaluated through galvanostatic charge-discharge measurements. In **Figure 8**, the overlap of galvanostatic discharge (Li^+ insertion) and charge (Li+ extraction) voltage profiles is depicted for $Co_4(HTrz)_2(D\text{-}cam)_{2.5}(\mu\text{-}OH)_3$-based batterie cathode material, operated at a current density of 50 mA·g^{-1} within the voltage range of 3.5 to 1.5 V vs. Li$^+$/Li. Based on the following figure, it is evident that the MOF cathode exhibits higher electroactivity, as associated with a higher initial discharge capacity of 301 mAh·g^{-1}.

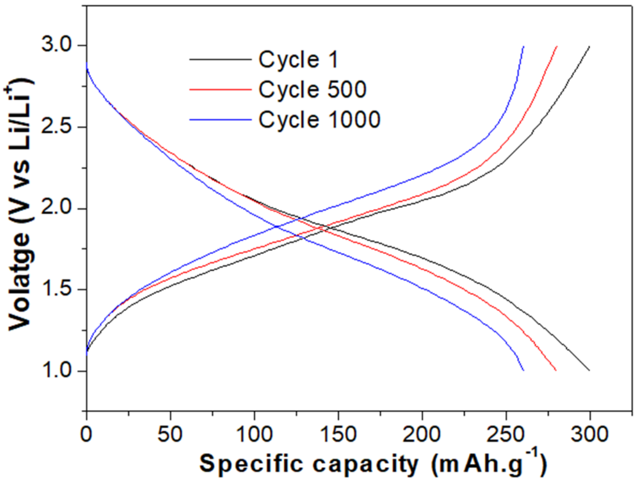

Figure 8. Galvanostatic charge-discharge curves of $Co_4(HTrz)_2(D\text{-}cam)_{2.5}(\mu\text{-}OH)_3$ MOF at different cycles.

In order to evaluate the $Co_4(HTrz)_2(D\text{-}cam)_{2.5}(\mu\text{-}OH)_3$ cathode's stability and durability in terms of specific capacity, extended cycle experiments are conducted at a constant current density of 50 mA g-1 between 3.0 and 1.0 V vs. Li^+/Li (**Fig. 9**). In terms of specific capacity, the repetitive cycling demonstrated good cyclability and stability for up to 100 cycles. Nevertheless, a discharge capacity of 267 mAh.g-1 is delivered for this new cathode at the 1000th cycle, which is an 11% reduction from the initial capacity of 301 mAh.g^{-1}. The process' reversibility is depicted through Coulombic efficiency, defined as the ratio of Q_{red} (the quantity of charge during reduction) to Q_{ox} (the quantity of charge during oxidation): Q_{red}/Q_{ox}, maintaining close proximity to 99% (**Fig. 9**). This signifies that all the lithium-ion intercalation into the cathode complex during the reduction process is completely expelled after the oxidation of the electrode as well as a complete reversibility in the Li^+ intercalation/de-intercalation under these conditions.

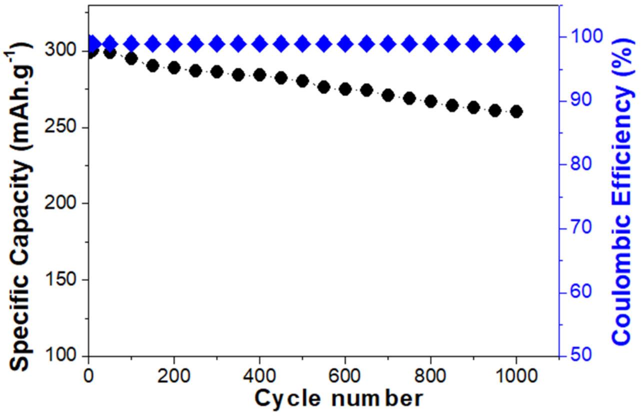

Figure 9. Specific capacity and coulombic efficiency evolution of $Co_4(HTrz)_2(D\text{-}cam)_{2.5}(\mu\text{-}OH)_3$ cathode with the number of cycles.

For an in-depth exploration of their rate performances, various current densities ranging from 50 to 300 mA/g were applied to assess the cathode cobalt complex, as depicted in **Figure 10**.

At current densities of 50, 100, 200, and 300 mA/g, the $Co_4(HTrz)_2(D\text{-}cam)_{2.5}(\mu\text{-}OH)_3$ cathode MOF demonstrates discharge capacities of 301, 260, 230, and 199 mAh/g, respectively. Importantly, a stable discharge capacity of 301 mAh/g is recoverable when the current density is returned to 50 mA/g, indicating the robust structural stability of the investigated sample after a high-rate discharge and charge cycles.

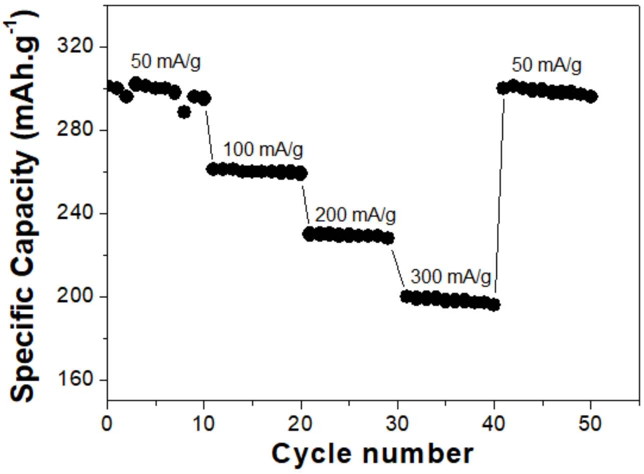

Figure 10. Rate capabilities of $Co_4(HTrz)_2(D\text{-}cam)_{2.5}(\mu\text{-}OH)_3$ composite cathode at various current densities.

To gain deeper insights into the electrode reaction kinetics of the $Co_4(HTrz)_2(D\text{-}cam)_{2.5}(\mu\text{-}OH)_3$ composite cathode MOF, Electrochemical impedance spectroscopy (EIS) analysis were conducted over a wide frequency range from 0.1 Hz to 100 kHz. It is to be noticed that EIS is a useful technique for evaluating the electrode sample's impedance response and the diffusion coefficient of Li^+ ions. The electrochemical impedance spectroscopy plots of the $Co_4(HTrz)_2(D\text{-}cam)_{2.5}(\mu\text{-}OH)_3$ cathode material are depicted in **Figure 11. a**. It is to be noticed that the plots were gathered during the discharge step, using an open-circuit potential. it is evident the Nyquist plots feature a minor intercept in the high-frequency region, two curved sections that partially overlap in the high- and medium-frequency ranges, as well as a linear segment in the low-frequency region. Additionally, the inset of this figure illustrates the equivalent circuit employed for acquiring the electrochemical impedance spectrum data. In this case, R_s denotes the collective resistance of the electrolyte, separator, and electrode. R_{ct} represents the charge transfer resistance, while Z_W accounts for the Warburg impedance, associated with the solid-state diffusion of ions in the active material and reflected in the sloping line observed in the low-frequency region. CPE signifies the capacitance arising from ion transfer within the active material.

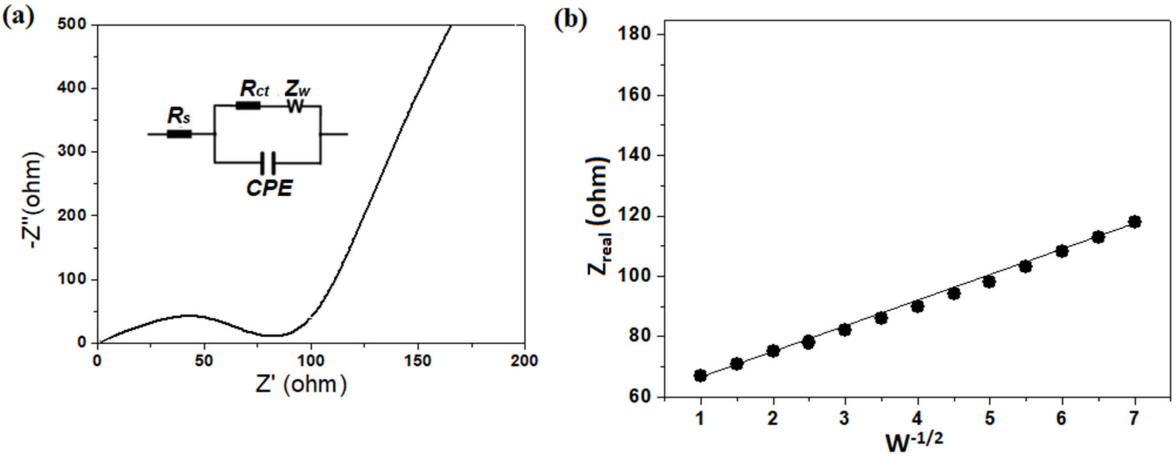

Figure 11. **(a)** The Nyquist plots, with the corresponding inset showcasing the fitted equivalent circuit model, including R_s (ohmic resistance of solution and electrodes), R_{ct} (charge transfer resistance), CPE (double-layer capacitance), and Z_w (Warburg impedance)**.** **(b)** Variation of Z_{real} aas a function of $w^{-1/2}$ of the $Co_4(HTrz)_2(D\text{-}cam)_{2.5}(\mu\text{-}OH)_3$ composite cathode.

The obtained fitting parameters reveal that the charge transfer resistance (R_{ct}) for the $Co_4(HTrz)_2(D\text{-}cam)_{2.5}(\mu\text{-}OH)_3$ composite cathode is 46.5 Ω. The estimation of the apparent diffusion coefficient of Li+ ions (D_{Li+}) can be derived from the low-frequency regions of the plots using the following two equations:

$$D_{Li+}= R^2T^2 /2S^2n^4F^4C2\boldsymbol{\sigma}^2 \qquad \text{(eq.6)}$$

$$Z'= R_s +R_{ct}+\boldsymbol{\sigma}_W\ w^{-1/2} \qquad \text{(eq.7)}$$

where R is the gas constant, T stands for the absolute temperature, S is attributed to the surface area of the electrode, n represents the number of electrons per molecule during oxidation, F is the Faraday constant, C is the concentration of Li^+, and σ is the Warburg impedance factor, which can be obtained by eq 1. Based on the slopes of the linear relationship between Z′ and $\omega^{-1/2}$ in the low frequency region displayed in **Figure 11. b**, the D_{Li+} of $Co_4(HTrz)_2(D\text{-}cam)_{2.5}(\mu\text{-}OH)_3$ composite cathode composite was 3.75×10^{-10} $cm^2.s^{-1}$.

In the given equations, R represents the gas constant, S is associated with the surface area of the electrode, T denotes the absolute temperature, n signifies the number of electrons per molecule during oxidation, F is the Faraday constant, C is the concentration of Li^+, and σ is the Warburg impedance factor. It is to be noticed that the value of σ can be determined using equation 1. By analyzing the slopes of the linear relationship between Z′ and $\omega^{-1/2}$ in the low-frequency region, as illustrated in **Figure 11. b**, the calculated D_{Li+} of $Co_4(HTrz)_2(D\text{-}cam)_{2.5}(\mu\text{-}OH)_3$ composite cathode was found to be 3.75×10^{-10} $cm^2.s^{-1}$.

IV. CONCLUSION

In summary, a novel tetra-nuclear mixed-ligand Co(II)-based MOF has been synthesized under hydrothermal conditions and fully characterized through several techniques. The SCXRD study reveals an overall 3-D porous helical network. The topological analysis of this porous MOF yields an unprecedented (4,3)-connected topology and a point symbol of $(3^{12}4^{18}5^{6})$ $(3^{9}4^{16}5^{3})$ based upon tetra-nuclear Co(II) clusters. The potential void space and large specific surface area were confirmed through the nitrogen adsorption/desorption isotherm measured at 77 K. Furthermore, the value of the gap energy was found to be 3.7 eV, suggesting the semi-conducting nature of the Co(II)-based material. When tested as cathode material, the Co-MOF exhibited significant electro-activity, demonstrating a high initial discharge capacity of 301 $mAh\cdot g^{-1}$ at a current density of 50 $mA\cdot g^{-1}$ within the voltage range of 3.5 to 1.5 V vs. Li^+/Li. Impressively, over 100 cycles, the material displayed high stability and cyclability regarding the specific capacity under a current density of 50 $mA\cdot g^{-1}$, with a reversibility close to 99%. These results suggest that the current investigation lays the groundwork for designing novel porous MOF materials that could serve as promising candidates for rechargeable Lithium-ion Batteries (LIBs). Furthermore, it expands the scope of such materials for applications in the development of clean and renewable solar cells and the production of new electromagnetic devices.

▪ ASSOCIATED CONTENT

Supporting Information: Crystallographic tables, SEM pictures and TGA curve, Infrared spectrum (PDF).

Supplementary crystallographic data for this article in CIF format are available as electronic supplementary publication from Cambridge Crystallographic Data Centre (CCDC: 2266912). This data can be obtained free of charge via https://www.ccdc.cam.ac.uk/community/deposita structure/CSD Communications/, or from the Cambridge Crystallographic Data Centre, 12 Union Road, Cambridge CB2 1EZ, UK (Fax: (international): +441223/336033; e-mail: deposit @ ccdc.cam.ac.uk

Abriviation

MOF: Metal organic framework

HTrz: 1H-1,2,4 Triazole

D-cam : (1R,3S)-(+)-Camphoric acid

Declaration of competing interest

The authors declare no competing financial interest.

Author contributions:

Dhouha ABID: characterization, writing, original draft, methodology, data curation, conceptualization. **Issam MJEJRI**: Conceptualization, characterization, data curation, writing, validation. **Rim JABALLI**: characterization, Methodology. **Philippe GUIONNEAU** : Validation, investigation, supervision. **Stanislav PECHEV** : Validation, investigation, supervision. **El kebir HLIL:** Validation, investigation, supervision. **Nathalie DARO**: Validation, investigation, supervision. **Zakaria ELAOUD**: Review, supervision, editing, methodology.

Additional information

Competing financial interests

The authors declare no competing financial interest

Highlights

- A new Co(II)-based MOF was synthesized through hydrothermal conditions using D-camphoric acid and N-donnor HTrz ligands.
- Crystal packing consists of an unusual periodic double left-right handed helical crystal and featured as an extended 3D porous framework.
- Potential void space and large specific surface area have been proved through the nitrogen adsorption/desorption isotherm.
- The electrochemical analysis demonstrated an excellent reversibility, cyclability, and structural stability in terms of specific capacity.

REFERENCES

1. Lv, Z., Li, W., Wei, J., Ho, F., Cao, J., & Chen, X. (2023). Autonomous Chemistry Enabling Environment-Adaptive Electrochemical Energy Storage Devices. CCS Chemistry, 5(1), 11–29. https://doi.org/10.31635/CCSCHEM.022.202202153
2. Bhattacharjee, U., Ghosh, S., Bhar, M., & Martha, S. K. (2023). Electrochemical energy storage part I: development, basic principle and conventional systems. Emerging Trends in Energy Storage Systems and Industrial Applications, 151–188. https://doi.org/10.1016/B978-0-323-90521-3.00001-6
3. Zhang, X., Li, L., Fan, E., Xue, Q., Bian, Y., Wu, F., & Chen, R. (2018). Toward sustainable and systematic recycling of spent rechargeable batteries. Chemical Society Reviews, 47(19), 7239–7302. https://doi.org/10.1039/c8cs00297e
4. Sakka, Y.; Yamashige, H.; Watanabe, A.; Takeuchi, A.; Uesugi, M.; Uesugi, K.; Orikasa, Y. Pressure Dependence on the Three-Dimensional Structure of a Composite Electrode in an All-Solid-State Battery. *J. Mater. Chem. A* 2022, *10* (31), 16602–16609. https://doi.org/10.1039/d2ta02378d.
5. Aurbach, D., Markevich, E., & Salitra, G. (2021). High Energy Density Rechargeable Batteries Based on Li Metal Anodes. The Role of Unique Surface Chemistry Developed in Solutions Containing Fluorinated Organic Co-solvents. Journal of the American Chemical Society, 143(50), 21161–21176. https://doi.org/10.1021/JACS.1C11315
6. Geng, J., Ni, Y., Zhu, Z., Wu, Q., Gao, S., Hua, W., Indris, S., Chen, J., & Li, F. (2022). Reversible Metal and Ligand Redox Chemistry in Two-Dimensional Iron-Organic Framework for Sustainable Lithium-Ion Batteries. Journal of the American Chemical Society. https://doi.org/10.1021/JACS.2C08273
7. Bhattacharjee, U., Bhowmik, S., Ghosh, S., & Martha, S. K. (2022). Effect of in-situ derived sulfur dispersion on dual carbon lithium-ion capacitors. Journal of Power Sources, 542. https://doi.org/10.1016/j.jpowsour.2022.231768
8. Bhattacharjee, U., Bhowmik, S., Ghosh, S., Vangapally, N., & Martha, S. K. (2022). Boron-doped graphene anode coupled with microporous activated carbon cathode for lithium-ion ultracapacitors. Chemical Engineering Journal, 430. https://doi.org/10.1016/j.cej.2021.132835
9. Sarode, K. K., Choudhury, R., & Martha, S. K. (2018). Binder and conductive additive free silicon electrode architectures for advanced lithium-ion batteries. Journal of Energy Storage, 17, 417–422. https://doi.org/10.1016/j.est.2018.04.002

10. Cao, B., Fang, H. T., Li, D., & Chen, Y. (2022). Controlled Synthesis of Single-Crystalline Ni-Rich Cathodes for High-Performance Lithium-Ion Batteries. ACS Applied Materials and Interfaces, 14(48), 53667–53676. https://doi.org/10.1021/ACSAMI.2C13832
11. Fan, Q., Zuba, M. J., Zong, Y., Menon, A. S., Pacileo, A. T., Piper, L. F. J., Zhou, G., & Liu, H. (2022). Surface Reduction Stabilizes the Single-Crystalline Ni-Rich Layered Cathode for Li-Ion Batteries. ACS Applied Materials and Interfaces, 14(34), 38795–38806. https://doi.org/10.1021/ACSAMI.2C09937
12. Mjejri, I., Etteyeb, N., & Sediri, F. (2014b). Vanadium oxides nanostructures: Hydrothermal synthesis and electrochemical properties. Materials Research Bulletin, 60, 97–104. https://doi.org/10.1016/j.materresbull.2014.08.015
13. Li, W., Asl, H. Y., Xie, Q., & Manthiram, A. (2019). Collapse of LiNi1- x- yCoxMnyO2 Lattice at Deep Charge Irrespective of Nickel Content in Lithium-Ion Batteries. Journal of the American Chemical Society, 141(13), 5097–5101. https://doi.org/10.1021/JACS.8B13798/SUPPL_FILE/JA8B13798_SI_001.PDF
14. Alsherari, S. A., Janene, F., Moulahi, A., Shili, H., Alnhas, I., & Mjejri, I. (2023). Vanadium oxide nanocomposite as electrode materials for lithium-ion batteries with high specific discharge capacity and long cycling life. Ionics, 29(1), 61–70. https://doi.org/10.1007/s11581-022-04811-0
15. Mjejri, I., Doherty, C. M., Rubio-Martinez, M., Drisko, G. L., & Rougier, A. (2017). Double-Sided Electrochromic Device Based on Metal-Organic Frameworks. ACS Applied Materials and Interfaces, 9(46), 39930–39934. https://doi.org/10.1021/acsami.7b13647
16. Park, K. S., Benayad, A., Kang, D. J., & Doo, S. G. (2008). Nitridation-driven conductive Li4Ti5O12 for lithium ion batteries. Journal of the American Chemical Society, 130(45), 14930–14931. https://doi.org/10.1021/JA806104N
17. Mjejri, I., Rougier, A., & Gaudon, M. (2017). Low-Cost and Facile Synthesis of the Vanadium Oxides V2O3, VO2, and V2O5 and Their Magnetic, Thermochromic and Electrochromic Properties. Inorganic Chemistry, 56(3), 1734–1741. https://doi.org/10.1021/acs.inorgchem.6b02880
18. Ober, S., Mesnier, A., & Manthiram, A. (2023). Surface Stabilization of Cobalt-Free LiNiO2with Niobium for Lithium-Ion Batteries. ACS Applied Materials and Interfaces. https://doi.org/10.1021/ACSAMI.2C20268
19. Liu, H., Li, W., Shen, D., Zhao, D., & Wang, G. (2015). Graphitic Carbon Conformal Coating of Mesoporous TiO2 Hollow Spheres for High-Performance Lithium Ion Battery Anodes. Journal of the American Chemical Society, 137(40), 13161–13166. https://doi.org/10.1021/jacs.5b08743
20. Shi, L., Chen, K., Du, R., Bachmatiuk, A., Rümmeli, M. H., Xie, K., Huang, Y., Zhang, Y., & Liu, Z. (2016). Scalable Seashell-Based Chemical Vapor Deposition Growth of Three-Dimensional Graphene Foams for Oil-Water Separation. Journal of the American Chemical Society, 138(20), 6360–6363. https://doi.org/10.1021/jacs.6b02262
21. Qin, J., He, C., Zhao, N., Wang, Z., Shi, C., Liu, E. Z., & Li, J. (2014). Graphene networks anchored with Sn@Graphene as lithium ion battery anode. ACS Nano, 8(2), 1728–1738. https://doi.org/10.1021/nn406105n
22. Guo, Y., Zeng, X., Zhang, Y., Dai, Z., Fan, H., Huang, Y., Zhang, W., Zhang, H., Lu, J., Huo, F., & Yan, Q. (2017). Sn Nanoparticles Encapsulated in 3D Nanoporous Carbon Derived from a Metal-Organic Framework for Anode Material in Lithium-Ion Batteries. ACS Applied Materials and Interfaces, 9(20), 17172–17177. https://doi.org/10.1021/acsami.7b04561
23. Liu, H., Li, W., Shen, D., Zhao, D., & Wang, G. (2015). Graphitic Carbon Conformal Coating of Mesoporous TiO2 Hollow Spheres for High-Performance Lithium Ion Battery Anodes. Journal of the American Chemical Society, 137(40), 13161–13166. https://doi.org/10.1021/jacs.5b08743
24. Wang, T., Kim, H. K., Liu, Y., Li, W., Griffiths, J. T., Wu, Y., Laha, S., Fong, K. D., Podjaski, F., Yun, C., Kumar, R. V., Lotsch, B. V., Cheetham, A. K., & Smoukov, S. K. (2018). Bottom-up Formation of Carbon-Based Structures with Multilevel Hierarchy from MOF-Guest Polyhedra. Journal of the American Chemical Society, 140(19), 6130–6136. https://doi.org/10.1021/jacs.8b02411

25. Gu, S., Bai, Z., Majumder, S., Huang, B., & Chen, G. (2019). Conductive metal–organic framework with redox metal center as cathode for high rate performance lithium ion battery. Journal of Power Sources, 429(May), 22–29. https://doi.org/10.1016/j.jpowsour.2019.04.087
26. Jiang, Y., Zhao, H., Yue, L., Liang, J., Li, T., Liu, Q., Luo, Y., Kong, X., Lu, S., Shi, X., Zhou, K., & Sun, X. (2021). Recent advances in lithium-based batteries using metal organic frameworks as electrode materials. Electrochemistry Communications, 122(November 2020), 106881. https://doi.org/10.1016/j.elecom.2020.106881
27. Kaveevivitchai, W., & Jacobson, A. J. (2015). Exploration of vanadium benzenedicarboxylate as a cathode for rechargeable lithium batteries. Journal of Power Sources, 278, 265–273. https://doi.org/10.1016/j.jpowsour.2014.12.094
28. Lang, X., Wang, X., Liu, Y., Cai, K., Li, L., & Zhang, Q. (2021). Cobalt-based metal organic framework (Co-MOFs)/graphene oxide composites as high-performance anode active materials for lithium-ion batteries. International Journal of Energy Research, 45(3), 4811–4820. https://doi.org/10.1002/er.6080
29. Li, C., Zhang, C., Xie, J., Wang, K., Li, J., & Zhang, Q. (2021). Ferrocene-based metal-organic framework as a promising cathode in lithium-ion battery. Chemical Engineering Journal, 404(June 2020), 126463. https://doi.org/10.1016/j.cej.2020.126463
30. Li, H., Ma, Y., Zhang, H., Diemant, T., Behm, R. J., Varzi, A., & Passerini, S. (2020). Metal–Organic Framework Derived Fe7S8 Nanoparticles Embedded in Heteroatom-Doped Carbon with Lithium and Sodium Storage Capability. Small Methods, 4(12), 1–12. https://doi.org/10.1002/smtd.202000637
31. Rambabu, D., Lakraychi, A. E., Wang, J., Sieuw, L., Gupta, D., Apostol, P., Chanteux, G., Goossens, T., Robeyns, K., & Vlad, A. (2021). An Electrically Conducting Li-Ion Metal-Organic Framework. Journal of the American Chemical Society, 143(30), 11641–11650. https://doi.org/10.1021/jacs.1c04591
32. Weng, Y. G., Yin, W. Y., Jiang, M., Hou, J. Le, Shao, J., Zhu, Q. Y., & Dai, J. (2020). Tetrathiafulvalene-Based Metal-Organic Framework as a High-Performance Anode for Lithium-Ion Batteries. ACS Applied Materials and Interfaces, 12(47), 52615–52623. https://doi.org/10.1021/acsami.0c14510
33. Zhou, J., Yang, Q., Xie, Q., Ou, H., Lin, X., Zeb, A., Hu, L., Wu, Y., & Ma, G. (2022). Recent progress in Co–based metal–organic framework derivatives for advanced batteries. Journal of Materials Science and Technology, 96, 262–284. https://doi.org/10.1016/j.jmst.2021.04.033
34. Li, X., Cheng, F., Zhang, S., & Chen, J. (2006). Shape-controlled synthesis and lithium-storage study of metal-organic frameworks Zn4O(1,3,5-benzenetribenzoate)2. Journal of Power Sources, 160(1), 542–547. https://doi.org/10.1016/j.jpowsour.2006.01.015
35. Gou, L., Hao, L. M., Shi, Y. X., Ma, S. L., Fan, X. Y., Xu, L., Li, D. L., & Wang, K. (2014). One-pot synthesis of a metal-organic framework as an anode for Li-ion batteries with improved capacity and cycling stability. Journal of Solid State Chemistry, 210(1), 121–124. https://doi.org/10.1016/j.jssc.2013.11.014
36. Yamada, T., Shiraishi, K., Kitagawa, H., & Kimizuka, N. (2017). Applicability of MIL-101(Fe) as a cathode of lithium ion batteries. Chemical Communications, 53(58), 8215–8218. https://doi.org/10.1039/c7cc01712j
37. Liu, Q., Yu, L., Wang, Y., Ji, Y., Horvat, J., Cheng, M. L., Jia, X., & Wang, G. (2013). Manganese-based layered coordination polymer: Synthesis, structural characterization, magnetic property, and electrochemical performance in lithium-ion batteries. Inorganic Chemistry, 52(6), 2817–2822. https://doi.org/10.1021/ic301579g
38. Geng, J., Ni, Y., Zhu, Z., Wu, Q., Gao, S., Hua, W., Indris, S., Chen, J., & Li, F. (2022). Reversible Metal and Ligand Redox Chemistry in Two-Dimensional Iron-Organic Framework for Sustainable Lithium-Ion Batteries. Journal of the American Chemical Society. https://doi.org/10.1021/jacs.2c08273
39. Sheldrick, G. M. (1997). SHELXL-97, Progr. X-ray Cryst. Struct. Refinement; Gottingen Univ. Gottingen, Ger.
40. Farrugia, L.J. (1999) WinGX suite for small-molecule single-crystal crystallography. Journal of Applied Crystallography, 32, 837-838. http://dx.doi.org/10.1107/S0021889899006020

41. Sheldrick, (2018), G. M. SHELXL-2018/1, Program for Crystal Structure Refinement University of Göttingen: Germany.
42. K, B. Diamond Version 4, 0, Impact GbR, Bonn, Germany (2009).
43. Chioma, F.; Ekennia, A. C.; Ibeji, C. U.; Okafor, S. N.; Onwudiwe, D. C.; Osowole, A. A.; Ujam, O. T. (2018), Synthesis, Characterization, Antimicrobial Activity and DFT Studies of 2-(Pyrimidin-2-Ylamino)Naphthalene-1,4-Dione and Its Mn(II), Co(II), Ni(II) and Zn(II) Complexes. Journal of Molecular Structure, 1163 (Ii), 455–464. https://doi.org/10.1016/j.molstruc.2018.03.025.
44. Huang, W.; Liu, T.; Wu, D.; Cheng, J.; Ouyang, Z. W.; Duan, C. (2013). Field-Induced Slow Relaxation of Magnetization in a Tetrahedral Co(Ii) Complex with Easy Plane Anisotropy. Dalton Transactions, 42 (43), 15326–15331. https://doi.org/10.1039/c3dt51801a.
45. Kilinç, D.; Saka, C.; Şahin, Ö. (2012). Hydrogen Generation from Catalytic Hydrolysis of Sodium Borohydride by a Novel Co(II)-Cu(II) Based Complex Catalyst. Journal of Power Sources, 217, 256–261. https://doi.org/10.1016/j.jpowsour.2012.06.018.
46. Singh, U. P.; Narang, S.; Pachfule, P.; Banerjee, R. (2014) Variation of CO2 Adsorption in Isostructural Cd(Ii)/Co(Ii) Based MOFs by Anion Modulation. CrystEngComm, 16 (23), 5012–5020. https://doi.org/10.1039/c4ce00058g.
47. Wang, J.; Yang, M.; Dong, W.; Jin, Z.; Tang, J.; Fan, S.; Lu, Y.; Wang, G. (2016). Co(II) Complexes Loaded into Metal-Organic Frameworks as Efficient Heterogeneous Catalysts for Aerobic Epoxidation of Olefins. Catalysis Science and Technology, 6 (1), 161–168. https://doi.org/10.1039/c5cy01099c.
48. Feng, L.; Zhou, M.; Ye, F.; Chen, C.; Hou, H. (2019). Water Adsorption and Proton Conduction of a Cobalt(II) Complex Assembled by Triazine-Based Polycarboxylate. Dalton Transactions, 48 (40), 15192–15197. https://doi.org/10.1039/c9dt03038g.
49. Kim, J.; Chen, B.; Reineke, T. M.; Li, H.; Eddaoudi, M.; Moler, D. B.; O'Keeffe, M.; Yaghi, O. M. (2001). Assembly of Metal-Organic Frameworks from Large Organic and Inorganic Secondary Building Units: New Examples and Simplifying Principles for Complex Structures. Journal of the American Chemical Society, 123 (34), 8239–8247. https://doi.org/10.1021/ja010825o.
50. Banerjee, R.; Phan, A.; Wang, B.; Knobler, C.; Furukawa, H.; O'Keeffe, M.; Yaghi, O. (2008). M. High-Throughput Synthesis of Zeolitic Imidazolate Frameworks and Application to CO2 Capture. Science, 319 (5865), 939–943. https://doi.org/10.1126/science.1152516.
51. Abid, D., Dhouib, I., Guionneau, P., Pechev, S., Chaabane, I., Daro, N., & Elaoud, Z. (2020). Proton conduction study of a new selenate-based hybrid compound. Journal of Alloys and Compounds, 824, 153826. https://doi.org/10.1016/j.jallcom.2020.153826
52. Abid, D., Dhouib, I., Guionneau, P., Pechev, S., Chaabane, I., Daro, N., & Elaoud, Z. (2020). Proton conduction study of a new selenate-based hybrid compound. Journal of Alloys and Compounds, 824, 153826. https://doi.org/10.1016/j.jallcom.2020.153826
53. Dhouib, I., Abid, D., Ouasri, A., Guionneau, P., & Elaoud, Z. (2021). DFT computation, Hirshfeld surfaces analysis, non-linear optical and spectroscopic investigations of a novel non-centrosymmetric organic –inorganic hybrid material [(CH3CH2)4N]HSeO4(H2SeO4)2. Journal of Solid State Chemistry, 299(March), 122134. https://doi.org/10.1016/j.jssc.2021.122134
54. Hfidhi, N.; Korb, M.; Fitta, M.; Čižmár, E.; Lang, H.; Naïli, H. (2019). Magneto-Electronic Properties and Structural Features of Unusual Bis(μ-Aqua) Bis(μ-Sulfato) Bridges in Binuclear Cobalt-Based 4-Aminopyridine. Inorganica Chimica Acta, 484, 206–213. https://doi.org/10.1016/j.ica.2018.09.033.
55. Yuan, S.; Qin, J. S.; Su, J.; Li, B.; Li, J.; Chen, W.; Drake, H. F.; Zhang, P.; Yuan, D.; Zuo, J.; Zhou, H. C. Sequential Transformation of Zirconium(IV)-MOFs into Heterobimetallic MOFs Bearing Magnetic Anisotropic Cobalt(II) Centers. Angew. Chemie - Int. Ed. 2018, 57 (38), 12578–12583. https://doi.org/10.1002/anie.201808568.
56. Yin, W.; Tao, C. A.; Zou, X.; Wang, F.; Qu, T.; Wang, J. The Tuning of Optical Properties of Nanoscale MOFs-Based Thin Film through Post-Modification. Nanomaterials 2017, 7 (9). https://doi.org/10.3390/nano7090242.

57. Yin, W.; Tao, C. an; Wang, F.; Huang, J.; Qu, T.; Wang, J. Tuning Optical Properties of MOF-Based Thin Films by Changing the Ligands of MOFs. Sci. China Mater. 2018, 61 (3), 391–400. https://doi.org/10.1007/s40843-017-9143-5.
58. Treger, M.; Hannebauer, A.; Schaate, A.; Budde, J. L.; Behrens, P.; Schneider, A. M. Tuning the Optical Properties of the Metal-Organic Framework UiO-66 via Ligand Functionalization. Phys. Chem. Chem. Phys. 2023, 25 (8), 6333–6341. https://doi.org/10.1039/d2cp03746g.
59. Fumanal, M.; Corminboeuf, C.; Smit, B.; Tavernelli, I. Optical Absorption Properties of Metal-Organic Frameworks: Solid State: Versus Molecular Perspective. Phys. Chem. Chem. Phys. 2020, 22 (35), 19512–19521. https://doi.org/10.1039/d0cp03899g.
60. Fumanal, M.; Corminboeuf, C.; Smit, B.; Tavernelli, I. Optical Absorption Properties of Metal-Organic Frameworks: Solid State: Versus Molecular Perspective. Phys. Chem. Chem. Phys. 2020, 22 (35), 19512–19521. https://doi.org/10.1039/d0cp03899g.
61. Heum, J.; Woo, Y.; Lee, R.; Tae, J.; Lee, G. Design and Synthesis of Novel Lanthanide MOFs by Unique in Situ Organic and Inorganic Reactions. 2022, 43(9), 1136–1140. https://doi.org/10.1002/bkcs.12592.
62. Anderson, S. L.; Tiana, D.; Ireland, C. P.; Capano, G.; Fumanal, M.; Gladysiak, A.; Kampouri, S.; Rahmanudin, A.; Guijarro, N.; Sivula, K.; Stylianou, K. C.; Smit, B. Taking Lanthanides out of Isolation: Tuning the Optical Properties of Metal-Organic Frameworks. Chem. Sci. 2020, 11 (16), 4164–4170. https://doi.org/10.1039/d0sc00740d.

Graphic for manuscript

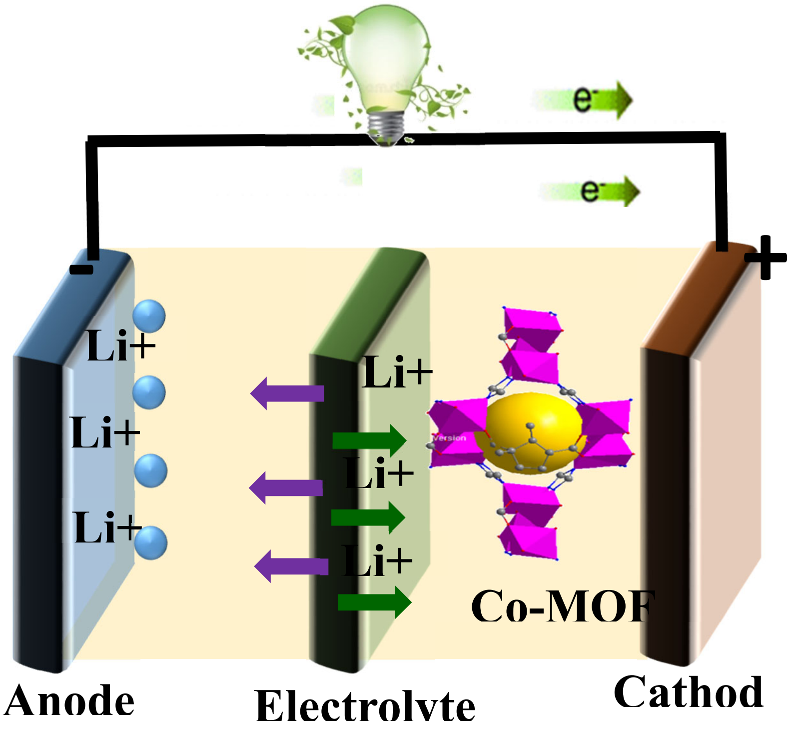

The synthesized porous mixed-ligand Co-MOF exhibits exceptional electrochemical performance with high initial discharge capacity, stability, and cyclability, achieving a reversibility of nearly 99%. The material's extensive surface area and porosity make it a promising candidate for environmentally friendly rechargeable lithium-ion batteries, opening avenues for the design of novel porous MOF materials.